Lawrence Berkeley National Laboratory

Title
Mitigation of microbunching instability in x-ray free electron laser linacs

Authors
Li, Biaobin
Qiang, Ji

Mitigation of microbunching instability in x-ray free electron laser linacs

Biaobin Li[1,2] and Ji Qiang[2,*]

[1]*National Synchrotron Radiation Laboratory, University of Science and Technology of China, Hefei, Anhui 230029, China*
[2]*Lawrence Berkeley National Laboratory, Berkeley, California 94720, USA*

(Received 9 September 2019; published 9 January 2020)

The microbunching instability seeded by small initial density modulation and driven by collective effects can cause significant electron beam quality degradation in next generation x-ray free electron lasers. A method exploiting longitudinal mixing derived from the natural transverse spread of the electron beam through a dispersive bending magnet was proposed to suppress this instability several years ago [Phys. Rev. Lett. **111**, 054801 (2013)]. Instead of using bending magnets to introduce the transverse-to-longitudinal coupling, which will lead to an inconvenient deflection of the downstream beam line, in this paper, we propose a scheme to mitigate the microbunching instability by inserting a quadrupole magnet inside a bunch compressor of the accelerator. This results in transverse-to-longitudinal phase space mixing and large slice energy spread that can efficiently mitigate the growth of the microbunching instability through the major accelerator section. Finally, at the exit of the accelerator, a dogleg section is used to restore the emittance and slice energy spread before entering the undulator radiation section. Multiparticle simulations show that the transverse space charge, structure wakefield, and the coherent synchrotron radiation effects will have a relatively small impact on this scheme.

I. INTRODUCTION

X-ray free electron lasers (FEL) provide an important tool for scientific discovery in physics, chemistry, biology, and material science. The performance of those x-ray FEL facilities critically depends on the electron beam quality out of linear accelerators, i.e., linacs. However, in the linear accelerator, due to the presence of collective effects such as the longitudinal space-charge effect, an initial small current density modulation inside an electron beam (e.g., from shot noise) will generate sufficiently large energy modulation of the beam after transporting through a section of the accelerator. The induced energy modulation will cause even larger density modulation inside the beam after passing through a magnetic bunch compressor to increase the electron beam peak current. This leads to the amplification of the initial density modulation, i.e., the microbunching instability. Typically, in a x-ray FEL linear accelerator, two stage magnetic bunch compressors or multiple stage magnetic bunch compressors are used to generate final high electron beam peak current. The microbunching instability will be dramatically amplified

through the accelerator and causes significant degradation of the electron beam quality at the entrance of undulator for x-ray radiation.

The microbunching instability was extensively studied in the past [1–14]. A conventional method to control the instability is to use a laser heater to increase the electron beam uncorrelated energy spread before bunch compression to damp the instability [4,5,15]. This is typically tolerable for the operation of self-amplified spontaneous emission (SASE) FELs. However, for seeded FELs it could degrade the FEL performance due to the increase of final electron beam energy spread [16]. Recently several new methods based on transverse-to-longitudinal coupling were proposed to suppress the microbunching instability [17–21]. These schemes are attractive because of the "reversible feature," which means the transverse emittance and slice energy spread can be recovered meanwhile effectively suppresses the microbunching instability [22]. So far, none of those methods has been applied to an entire linear accelerator system. The scheme based on two bending magnets [17] is a simple inexpensive method without using sophisticated hardware such as a rf cavity. However, the use of bending magnets changes the beam line direction, which is not convenient and difficult to apply to the existing FEL linacs.

In this paper, we propose a scheme to mitigate the microbunching instability by inserting a quadrupole magnet inside a four dipole bunch compressor chicane to allow dispersion leakage and transverse-to-longitudinal coupling

*[*]jqiang@lbl.gov

through the rest of the linac in a two-stage bunch compression accelerator. This method does not require the use of any new type of hardware in comparison to the other reversible methods and also keeps the original straight linac beam line geometry without changing direction. One effect of coupling is to smear out the already induced current or energy modulation before the bunch compressor. The other effect is to increase slice energy spread due to the presence of correlated energy chirp before the bunch compressor, which efficiently suppresses the microbunching instability in the following accelerator sections. At the end of the accelerator, a dogleg section is used to remove the dispersion and the coupling. By properly tuning the quadrupole strength inside the dogleg, one can obtain an achromatic lattice from the entrance of the bunch compressor to the exit of the dogleg. This removes the transverse-to-longitudinal coupling after the dogleg. Meanwhile, the increased emittance and slice energy spread are also restored.

The organization of the paper is as follows: after the Introduction, in Sec. II, we present the microbunching instability mitigation scheme with matrix formalism and corresponding linear optics design. In Sec. III, the analytical calculation of the microbunching instability gain is given and benchmarked with simulations. In Sec. IV, numerical simulations including space charge effects, coherent synchrotron radiation (CSR) and the accelerator transverse structure wakefield effects are presented. Finally, we draw conclusions in Sec. V.

II. MICROBUNCHING INSTABILITY MITIGATION SCHEME

We consider an x-ray FEL linear accelerator machine layout including the microbunching instability mitigation scheme as shown in Fig. 1. This accelerator includes three accelerating linac sections separated by two bunch compressor chicanes. One quadrupole is placed in the middle of bunch compressor one (BC1) to leak out the dispersion and longitudinal mixing terms R_{51} and R_{52} for instability mitigation. The energy chirp induced by Linac-2 is canceled by Linac-3. For energy chirp generated in Linac-1, it will be maintained after Linac-3, which calls for an isochronous dogleg design to avoid further bunch length compression. The final residual energy chirp is expected to
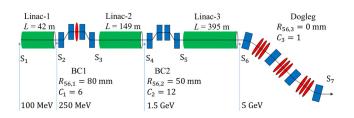
be removed by a dechirper [23,24] or resistive wall wakefield of further transport system.

The longitudinal phase space smearing brought up by the coupling terms in BC1 can greatly smooth the upstream density and energy modulation, thus suppresses further instability amplification in the following transport system. Meanwhile, due to the existence of energy chirp before BC1, additional slice energy spread will also be induced by the transverse to longitudinal coupling terms, which is given as [21,25]:

$$\sigma_\delta(s_3) \approx C_1 h_1 R_{51}^1 \sigma_x(s_2),\tag{1}$$

where C_1 is the compression factor from s_1 to s_3, h_1 and $\sigma_x(s_2)$ are the energy chirp and the horizontal rms beam size before BC1, R_{51}^1 is the coupling term from BC1 section. Substituting the lattice parameters shown in Fig. 1, assuming $R_{51}^1 = 0.05, \sigma_x(s_2) = 0.2$ mm, the resultant slice energy spread could be increased to about 156 keV, which is an order of magnitude larger than the nominal value (2 keV × 6 = 12 keV). Finally, at the exit of the accelerator, the extra slice energy spread and the transverse emittance growth can be removed by adjusting the quadrupoles inside the dogleg, which eliminates the induced couplings and makes the entire system an achromat.

The above accelerator system can be described using a transfer matrix approach. Here the linear transfer matrices from s_2 to s_7, written as $R = R^D T_r R^1$, in $(x, x' \equiv dx/ds, z, \delta)$ coordinates are given in the above scheme, where R^1 is the transfer matrix from $s_2 \to s_3$,

$$R^1 = \begin{pmatrix} R_{11}^1 & R_{12}^1 & 0 & R_{16}^1 \\ R_{21}^1 & R_{22}^1 & 0 & R_{26}^1 \\ R_{51}^1 & R_{52}^1 & 1 & R_{56,1} \\ 0 & 0 & 0 & 1 \end{pmatrix},\tag{2}$$

R^D is the transfer matrix of the dogleg section from $s_6 \to s_7$,

$$R^D = \begin{pmatrix} R_{11}^D & R_{12}^D & 0 & R_{16}^D \\ R_{21}^D & R_{22}^D & 0 & R_{26}^D \\ R_{51}^D & R_{52}^D & 1 & 0 \\ 0 & 0 & 0 & 1 \end{pmatrix},\tag{3}$$

T_r is the middle accelerator section from $s_3 \to s_6$

$$T_r = \begin{pmatrix} r_{11} & r_{12} & 0 & 0 \\ r_{21} & r_{22} & 0 & 0 \\ 0 & 0 & (1+\zeta)/C_2 & R_{56,2}\gamma_3/\gamma_5 \\ 0 & 0 & 0 & (C_2\gamma_3/\gamma_7)/(1+\zeta) \end{pmatrix},\tag{4}$$

where $\zeta = (C_1 - 1)C_2(R_{56,2}\gamma_3)/(R_{56,1}\gamma_5)$, γ_j is the beam relativistic factor at position s_j. By using the symplectic

FIG. 1.   A schematic layout of a x-ray FEL linac with two compression stages and the microbunching instability mitigation scheme.

condition of the transfer matrices ($R^T(s_{0\to 1}) \cdot S \cdot R(s_{0\to 1}) = S \cdot \gamma_0/\gamma_1$, when taking acceleration effects into account) and choosing the dogleg section so that

$$R_{51}^D = \frac{[r_{21}(R_{52}^1 R_{11}^1 - R_{51}^1 R_{12}^1) + r_{22}(R_{52}^1 R_{21}^1 - R_{51}^1 R_{22}^1)]}{C_2/(1+\zeta\gamma_7/\gamma_3)},$$

$$R_{52}^D = \frac{[-r_{11}(R_{52}^1 R_{11}^1 - R_{51}^1 R_{12}^1) - r_{12}(R_{52}^1 R_{21}^1 - R_{51}^1 R_{22}^1)]}{C_2/[(1+\zeta)\gamma_7/\gamma_3]},$$

(5)

the accelerator system from the entrance of BC1 to the exit of the dogleg section can be made as an achromat with the linear transfer matrix from s_2 to s_7

$$R_{s_2\to 7} = \begin{pmatrix} R_{11} & R_{12} & 0 & 0 \\ R_{21} & R_{22} & 0 & 0 \\ 0 & 0 & (1+\zeta)/C_2 & \frac{R_{56,1}}{C_2} + \frac{C_1 R_{56,2}\gamma_3}{\gamma_5} \\ 0 & 0 & 0 & \frac{C_2\gamma_3}{(1+\zeta)\gamma_7} \end{pmatrix}. \quad (6)$$

Following the schematic layout shown in Fig. 1, we did linear optics design based on the above first-order transfer map without including collective effects. In order to generate the coupling terms for the instability mitigation, one quadrupole is inserted at the center location of the bunch compressor chicane BC1. The normalized quadrupole strength of $0.83/m^2$ with 0.2 m length is used as an example, which leaks out $R_{51}^1 = 0.05$, $R_{52}^1 = 0.18$ m for the microbunching instability mitigation. The initial beam transverse distribution is a uniform round cross section with 0.4 mm radius and 0.3 μm normalized transverse emittance. The longitudinal electron position is uniformly distributed with a flattop current of 20 A. A Gaussian function is used for the electron energy distribution. The initial uncorrelated energy spread is 2 keV (rms) with zero energy chirp. The beam is accelerated from the initial 100 MeV at the entrance to Linac-1 to final 5 GeV with a total compression factor of 72. FODO structures are applied in each linac sections to control the beam size. The energy chirp induced in Linac-2 is canceled by Linac-3. The dogleg section, which consists of two dipole pair sandwiching three independent quadrupoles, is designed to be both isochronous and achromatic at the same time. The residual energy chirp from Linac-1 after the dogleg can be dechirped by additional beam line elements such as a dechirper. The beam and the lattice parameters are summarized in Table I.

The transverse beam size evolution without including collective effects is shown in Fig. 2. Starting from the location of BC1, the horizontal beam size increases significantly due to the leakage of dispersion. This dispersion is present through the Linac-2, the bunch compressor BC2, the

TABLE I.   Main parameters for the electron beam and lattice.

Parameter	Symbol	Value
Beam energy	$\gamma_0 mc^2$	100 MeV
Normalized emittance	$\epsilon_{x,n}, \epsilon_{y,n}$	0.3 μm
Beam radius	r_b	0.4 mm
Uncorrelated energy spread	σ_E	2 keV
Bunch current	I_0	20 A
Bunch charge	Q	330 pC
Bending angle of the dipole in BC1	θ_1	6.34°
Dipole length in BC1	L_b	0.2 m
Drift length between first two dipoles in BC1	L_d	2.5 m
Quadrupole strength in BC1	K_1	0.83 m^{-2}
Quadrupole length in BC1	L_q	0.2 m
Coupling terms of BC1	(R_{51}^1, R_{52}^1)	(0.05, 0.18 m)
Bending angle of the dipole in BC2	θ_2	5.57°
Dipole length in BC2	L_b	0.2 m
Drift length between first two dipoles in BC2	L_d	2.5 m
Bending angle of the dogleg	θ_3	1.15°

Linac-3 until the exit of the dogleg section. The transverse beam size at the entrance of BC1 is matched back to the initial beam radius 0.4 mm. Due to the leakage of dispersion from BC1, the beam horizontal size is much larger than the vertical beam size. The maximum rms beam size in rf cavities is about 2 mm which is within a reasonable limit of superconducting cavity aperture size to avoid potential beam loss to the cavity wall.

The emittance evolutions along the accelerator is shown in Fig. 3. Under the linear map transportation, the horizontal emittance is restored to the initial 0.3 mm mrad at the exit of dogleg by tuning the quadrupoles inside the dogleg section according to Eq. (5) with the help of optimization tools in ELEGANT [26].

The slice energy spread evolution when the quadrupole in BC1 is turned off and on is plotted in Fig. 4. It is seen that after the bunch compressor BC1, besides the slice energy
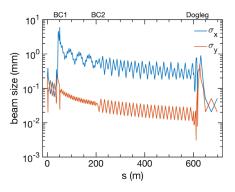

FIG. 2.   Evolution of the beam transverse rms size along the longitudinal position.
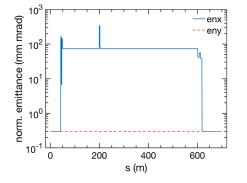
FIG. 3. Evolution of the beam transverse normalized emittance along the longitudinal position.
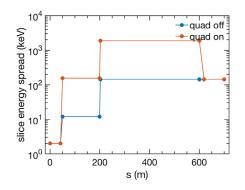

FIG. 4. Evolution of the beam slice energy spread along the longitudinal position when quadrupole in BC1 is turned off and on.

increase due to compression in the case of normal bunch compressor (blue plot in the figure), there is additional slice energy spread increase due to the transverse-to-longitudinal coupling when the quadrupole is turned on. The larger slice energy spread helps mitigate the amplification of micro-bunching instability through these sections. The final slice energy spread is restored to the normal increased energy spread 144 keV (a factor of 72 compression of initial 2 keV energy spread) at the exit of the dogleg section after the transverse-to-longitudinal coupling is removed and the entire system becomes an achromatic system.

III. MICROBUNCHING INSTABILITY GAIN

For the accelerator layout including the mitigation scheme shown in Fig. 1, we calculated microbunching instability gain at the exit of the dogleg section. Assuming an electron beam with an initial current modulation factor b_0 at the entrance (s_1) to Linac-1, the modulation factor at a location s of the accelerator can be obtained by solving the following integral equation [2,3]:

$$b[k(s); s] = b_0[k(s); s] + \int_{s_0}^{s} K(\tau, s) b[k(\tau); \tau] d\tau \quad (7)$$

where the kernel of the above integral equation is given as:

$$K(\tau; s) = ik(s)\hat{R}_{56}(\tau \to s)\frac{I(\tau)}{I_A}\frac{Z[k(\tau); \tau]}{\gamma_0}\exp\left(-\frac{k_0^2}{2}U^2\sigma_{\delta 0}^2\right)$$

$$\times \exp\left(\frac{-k_0^2\epsilon_{x0}}{2\gamma_0\beta_{x0}}T\right) \quad (8)$$

with the Alfvén current $I_A \simeq 17.045$ kA.

By iterating the above integral equation three times, neglecting collective effects inside the two bunch compressors and the dogleg, we obtain the final modulation factor at the exit (s_7) of the dogleg as:

$$b[k(s_7); s_7]$$
$$= b_{01}[k(s_7); s_7]$$
$$+ b_{11}[k(s_7); s_7] + b_{12}[k(s_7); s_7] + b_{13}[k(s_7); s_7]$$
$$+ b_{21}[k(s_7); s_7] + b_{22}[k(s_7); s_7] + b_{23}[k(s_7); s_7]$$
$$+ b_{31}[k(s_7); s_7], \quad (9)$$

where $k(s) = C(s)k_0$ and $C(s)$ is the compression factor from s_1 to s, and k_0 is the initial modulation wave number. Here b_{01} denotes evolution of the modulation factor in the absence of all collective effects, and is given as:

$$b_{01}[k(s_7); s_7] = b_0 \exp[-k^2(s_7)\hat{R}_{56}^2(s_{1\to7})\sigma_{\delta_0}^2/2]; \quad (10)$$

The three terms of b_{11}, b_{12}, b_{13} denote amplification of the initial microbunching due to collective effects between the linac section of $s_{1\to2}$, $s_{3\to4}$, $s_{5\to6}$ respectively, and are given as:

$$b_{11}[k(s_7); s_7] = ib_0k(s_7)\hat{R}_{56}(s_{1\to7})\frac{I(s_1)}{\gamma_0}\hat{Z}(s_{1\to2})$$

$$\times \exp\left(\frac{-k_0^2\mathcal{D}^2(s_{1\to7})\sigma_{\delta_0}^2}{2}\right)$$

$$\times \exp\left(\frac{-k_0^2\mathcal{H}(s_{1\to7})\epsilon_{x,n}}{2\gamma_0\beta_{x0}}\right), \quad (11)$$

$$b_{12}[k(s_7); s_7] = ib_0k(s_7)\hat{R}_{56}(s_{3\to7})\frac{I(s_3)}{\gamma_0}\hat{Z}(s_{3\to4})$$

$$\times \exp\left(\frac{-k_0^2\mathcal{D}^2(s_{3\to7})\sigma_{\delta_0}^2}{2}\right)$$

$$\times \exp\left(\frac{-k_0^2\mathcal{H}(s_{3\to7})\epsilon_{x,n}}{2\gamma_0\beta_{x0}}\right), \quad (12)$$

$$b_{13}[k(s_7); s_7] = ib_0k(s_7)\hat{R}_{56}(s_{5\to7})\frac{I(s_5)}{\gamma_0}\hat{Z}(s_{5\to6})$$

$$\times \exp\left(\frac{-k_0^2\mathcal{D}^2(s_{5\to7})\sigma_{\delta_0}^2}{2}\right)$$

$$\times \exp\left(\frac{-k_0^2\mathcal{H}(s_{5\to7})\epsilon_{x,n}}{2\gamma_0}\beta_{x0}\right); \quad (13)$$

The following three terms b_{21}, b_{22}, b_{23} denote the two-stage coupling collective effects between the section $s_{1\to2}$ and $s_{3\to4}$, $s_{1\to2}$ and $s_{5\to6}$, $s_{3\to4}$ and $s_{5\to6}$ respectively, and are given as:

$$
\begin{aligned}
b_{21}[k(s_7);s_7] = &-b_0 k(s_3)k(s_7)\hat{R}_{56}(s_{1\to3})\hat{R}_{56}(s_{3\to7})\\
&\times \frac{I(s_1)I(s_3)}{(\gamma_0)^2}\hat{Z}(s_{1\to2})\hat{Z}(s_{3\to4})\\
&\times \exp\left(\frac{-k_0^2 \mathcal{D}^2(s_{1\to3\to7})\sigma_{\delta_0}^2}{2}\right)\\
&\times \exp\left(\frac{-k_0^2 \mathcal{H}(s_{1\to3\to7})\epsilon_{x,n}}{2\gamma_0\beta_{x0}}\right),
\end{aligned}
\tag{14}
$$

$$
\begin{aligned}
b_{22}[k(s_7);s_7] = &-b_0 k(s_5)k(s_7)\hat{R}_{56}(s_{1\to5})\hat{R}_{56}(s_{5\to7})\\
&\times \frac{I(s_1)I(s_5)}{(\gamma_0)^2}\hat{Z}(s_{1\to2})\hat{Z}(s_{5\to6})\\
&\times \exp\left(\frac{-k_0^2 \mathcal{D}^2(s_{1\to5\to7})\sigma_{\delta_0}^2}{2}\right)\\
&\times \exp\left(\frac{-k_0^2 \mathcal{H}(s_{1\to5\to7})\epsilon_{x,n}}{2\gamma_0\beta_{x0}}\right),
\end{aligned}
\tag{15}
$$

$$
\begin{aligned}
b_{23}[k(s_7);s_7] = &-b_0 k(s_5)k(s_7)\hat{R}_{56}(s_{3\to5})\hat{R}_{56}(s_{5\to7})\\
&\times \frac{I(s_3)I(s_5)}{(\gamma_0)^2}\hat{Z}(s_{3\to4})\hat{Z}(s_{5\to6})\\
&\times \exp\left(\frac{-k_0^2 \mathcal{D}^2(s_{3\to5\to7})\sigma_{\delta_0}^2}{2}\right)\\
&\times \exp\left(\frac{-k_0^2 \mathcal{H}(s_{3\to5\to7})\epsilon_{x,n}}{2\gamma_0\beta_{x0}}\right);
\end{aligned}
\tag{16}
$$

The last term denotes the three-stage coupling amplification due to the collective effects between the region $s_{1\to2}$ and $s_{3\to4}$ and $s_{5\to6}$, and are given as:

$$
\begin{aligned}
b_{31}[k(s_7);s_7] = &-ib_0 k(s_3)k(s_5)k(s_7)\hat{R}_{56}(s_{1\to3})\\
&\times \hat{R}_{56}(s_{3\to5})\hat{R}_{56}(s_{5\to7})\frac{I(s_1)I(s_3)I(s_5)}{(\gamma_0)^3}\\
&\times \hat{Z}(s_{1\to2})\hat{Z}(s_{3\to4})\hat{Z}(s_{5\to6})\\
&\times \exp\left(\frac{-k_0^2 \mathcal{D}^2(s_{1\to3\to5\to7})\sigma_{\delta_0}^2}{2}\right)\\
&\times \exp\left(\frac{-k_0^2 \mathcal{H}(s_{1\to3\to5\to7})\epsilon_{x,n}}{2\gamma_0\beta_{x0}}\right),
\end{aligned}
\tag{17}
$$

where σ_{δ_0} is the initial rms relative energy spread, γ_0 is the initial electron beam relativistic factor, $I(s_j) = C(s_j)I_0$, I_0 is the initial current. The impedance term in the above equations are defined as:

$$
\hat{Z}(s_{j\to k}) = \int_{s_j}^{s_k}\frac{4\pi Z[k(\tau);\tau]}{I_A Z_0}d\tau,
$$

where $Z[k(\tau);\tau]$ is the impedance per unit length of collective effects and Z_0 is the vacuum impedance. The exponential damping to the modulation amplification due to initial energy spread is given as:

$$
\begin{aligned}
\mathcal{D}^2(s_{1\to7}) &= U^2(s_7,s_1),\\
\mathcal{D}^2(s_{3\to7}) &= U^2(s_7,s_3) + U^2(s_3,s_1),\\
\mathcal{D}^2(s_{5\to7}) &= U^2(s_7,s_5) + U^2(s_5,s_1),\\
\mathcal{D}^2(s_{1\to3\to7}) &= U^2(s_7,s_3) + U^2(s_3,s_1),\\
\mathcal{D}^2(s_{1\to5\to7}) &= U^2(s_7,s_5) + U^2(s_5,s_1),\\
\mathcal{D}^2(s_{3\to5\to7}) &= U^2(s_7,s_5) + U^2(s_5,s_3) + U^2(s_3,s_1),\\
\mathcal{D}^2(s_{1\to3\to5\to7}) &= U^2(s_7,s_5) + U^2(s_5,s_3) + U^2(s_3,s_1),
\end{aligned}
\tag{18}
$$

where

$$
U(s,\tau) = C(s)\hat{R}_{56}(s) - C(\tau)\hat{R}_{56}(\tau). \tag{19}
$$

The damping effects due to transverse-to-longitudinal couplings are given as:

$$
\begin{aligned}
\mathcal{H}(s_{1\to7}) &= T(s_7,s_1),\\
\mathcal{H}(s_{3\to7}) &= T(s_7,s_3) + T(s_3,s_1),\\
\mathcal{H}(s_{5\to7}) &= T(s_7,s_5) + T(s_5,s_1),\\
\mathcal{H}(s_{1\to3\to7}) &= T(s_7,s_3) + T(s_3,s_1),\\
\mathcal{H}(s_{1\to5\to7}) &= T(s_7,s_5) + T(s_5,s_1),\\
\mathcal{H}(s_{3\to5\to7}) &= T(s_7,s_5) + T(s_5,s_3) + T(s_3,s_1),\\
\mathcal{H}(s_{1\to3\to5\to7}) &= T(s_7,s_5) + T(s_5,s_3) + T(s_3,s_1),
\end{aligned}
\tag{20}
$$

where

$$
T(s,\tau) = [\beta_{x0}V(s,\tau) - \alpha_{x0}W(s,\tau)]^2 + W(s,\tau)^2, \tag{21}
$$

where β_{x0} and α_{x0} are the initial horizontal Twiss parameters, V and W are defined as:

$$
\begin{aligned}
V(s,\tau) &= C(s)\hat{R}_{51}(s) - C(\tau)\hat{R}_{51}(\tau),\\
W(s,\tau) &= C(s)\hat{R}_{52}(s) - C(\tau)\hat{R}_{52}(\tau).
\end{aligned}
\tag{22}
$$

We used the shorthand notation $\hat{R}(s) = \hat{R}(s_1 \to s)$ here. In order to include acceleration effects, the transfer matrix terms are defined as [6]:

$$\hat{R}_{51}(s_{j\to k}) = R_{51}(s_{j\to k})\sqrt{\gamma_0/\gamma_j},$$

$$\hat{R}_{52}(s_{j\to k}) = R_{52}(s_{j\to k})\sqrt{\gamma_0/\gamma_j},$$

$$\hat{R}_{56}(s_{j\to k}) = R_{56}(s_{j\to k})\gamma_0/\gamma_j, \qquad (23)$$

where γ_j is the relativistic factor at location s_j.

For the convenience of the following benchmark, here we listed the transfer matrix terms based on Eq. (23). The momentum compaction factors along the accelerator beam line as shown in Fig. 1 are given as:

$$\hat{R}_{56}(s_{1\to 3}) = \frac{R_{56,1}\gamma_1}{\gamma_3},$$

$$\hat{R}_{56}(s_{1\to 5}) = \frac{R_{56,1}\gamma_1}{C_2\gamma_3} + \frac{R_{56,2}C_1\gamma_1}{\gamma_5},$$

$$\hat{R}_{56}(s_{1\to 7}) = \frac{R_{56,1}\gamma_1}{C_2\gamma_3} + \frac{R_{56,2}C_1\gamma_1}{\gamma_5},$$

$$\hat{R}_{56}(s_{3\to 5}) = \frac{R_{56,2}\gamma_1}{\gamma_5},$$

$$\hat{R}_{56}(s_{3\to 7}) = \frac{R_{56,2}\gamma_1}{\gamma_5},$$

$$\hat{R}_{56}(s_{5\to 7}) = 0. \qquad (24)$$

Applying the achromatic condition in Eq. (5), the transverse-to-longitudinal coupling terms are written as:

$$\hat{R}_{51}(s_{1\to 3}) \equiv \hat{R}_{51}^1 = m_{11}R_{51}^1 + m_{21}R_{52}^1,$$

$$\hat{R}_{52}(s_{1\to 3}) \equiv \hat{R}_{52}^1 = m_{12}R_{51}^1 + m_{22}R_{52}^1,$$

$$\hat{R}_{51}(s_{1\to 5}) = \hat{R}_{51}^1 \cdot \left[\frac{1}{C_2} + \frac{(C_1-1)\gamma_3 R_{56,2}}{\gamma_5 R_{56,1}}\right],$$

$$\hat{R}_{52}(s_{1\to 5}) = \hat{R}_{52}^1 \cdot \left[\frac{1}{C_2} + \frac{(C_1-1)\gamma_3 R_{56,2}}{\gamma_5 R_{56,1}}\right],$$

$$\hat{R}_{51}(s_{1\to 7}) = 0,$$

$$\hat{R}_{52}(s_{1\to 7}) = 0, \qquad (25)$$

where m_{ij} is the transfer matrix term in $(s_1 \to s_2)$ section. Here, we have used $(R_{56,3} = 0, C_3 = 1)$ in the above Eqs. (24) and (25). These equations suggest that the electron beam transverse size would affect the microbunching instability gain through the transverse-to-longitudinal coupling process, which can also be seen from Eq. (1).

To benchmark our analytical gain model, simulations using a multiparticle simulation code IMPACT [27,28] were also carried out. In the following calculation of microbunching instability gain, we included only longitudinal space-charge (LSC) effect to account for collective effects of electron beam through the accelerator since it is the dominant factor during the process of microbunching amplification [4]. The averaged free-space LSC impedance model based on round uniform electron beam is used in the analytical calculations which is given as [8]:

TABLE II. Average beam size (rms) in each linac section when quadrupole in BC1 is turned off.

Parameter	Value
Average (σ_x, σ_y) in Linac-1	(0.10, 0.10) mm
Average (σ_x, σ_y) in Linac-2	(0.05, 0.05) mm
Average (σ_x, σ_y) in Linac-3	(0.02, 0.02) mm

$$Z_{\text{avg}}(k) = \frac{iZ_0}{\pi\gamma r_b}\frac{1 - \zeta I_0(kr/\gamma)K_1(\zeta)}{\zeta}\bigg|_{\zeta=kr_b/\gamma}, \qquad (26)$$

where r_b is the beam radius, k is the wave number, γ is the relativistic factor, and I_1, K_1 are modified Bessel functions of the first kind. The initial electron beam distribution is same as the parameters listed in Table I except that the bunch length and the charge were changed according to the initial modulation wavelength for simulations in the low frequency spectrum range. To reduce the artificial numerical noise due to a small number of macroparticles (20 millions) in the simulations, a quiet loading method based on Halton sequence samplings was used [29]. A maximum 1024 longitudinal grid points were used in the simulations, which ensures 20 grid points per modulation wavelength.

First, we consider the case when the quadrupole in BC1 is turned off. The electron beam transportation between $(s_1 \to s_6)$ is considered, which corresponds to the conventional two-stage bunch compression linear accelerator. The accelerator lattice was tuned again to match the FODO structures in each linac section. The dipole strength in BC1 is also tuned to maintain the initial momentum compaction factor. The average beam size along the accelerator beam line is listed in Table II. Substituting the momentum compaction factors listed in Eq. (24) into Eq. (9) and setting all the transverse-to-longitudinal coupling terms listed in Eq. (25) to zeros, the microbunching gain at the exit of Linac-3 is the same as the gain at the exit of dogleg. The final microbunching gain $|b[k(s_6); s_6]/b_0|$ with different initial current modulation wavelength is shown in Fig 5.

We also calculated the microbunching instability gain in the above case using the IMPACT code. The simulation results are also shown in Fig. 5. The discrepancy between the theory and the simulation at short wavelength could be due to the difference between the 1D LSC impedance in the analytical model and the 3D LSC model in the macroparticle simulation. These two models show larger difference toward shorter wavelength region as reported in Ref. [8]).

When the quadrupole in BC1 is turned on to mitigate the microbunching instability, the final gain at the exit of the dogleg section was calculated using the above analytical model and the macroparticle simulation. The electron beam and accelerator lattice parameters listed in the previous linear optics design section are used. The final gain spectrum $|b[k(s_7); s_7]/b_0|$ from both the analytical model calculation and from the macroparticle simulation are shown in Fig 6. Comparing the microbunching instability gain in this case with that in the case of no quadrupole in
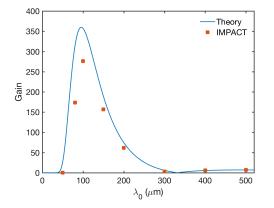
FIG. 5. Microbunching gain spectrum from the analytical model and from the numerical macroparticle simulation when the quadrupole in BC1 is turned off.
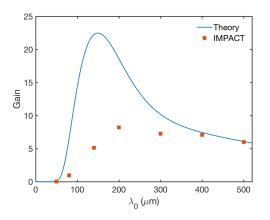

FIG. 6. Microbunching gain spectrum from the analytical model and from the numerical macroparticle simulation when the quadrupole in BC1 is turned on.

BC1, we see that the instability is efficiently mitigated with the use of the quadrupole in BC1. The maximum instability gain in the normal two-stage bunch compression linear accelerator is reduced by more than an order of magnitude. The residual microbunching gain is mainly due to the contribution from Eq. (11). Since the $(s_2 \rightarrow s_7)$ section is an achromat but with nonzero R_{56}, the energy modulations induced upstream before the BC1 can still be amplified. The instability gain from the simulation is less than that from the analytical model when the initial modulation wavelength is below 400 microns. This is because the electron beam is not a round beam but a flat beam ($\sigma_x \gg \sigma_y$) due to the dispersion leakage after the BC1.

TABLE III. Average beam size (rms) in each linac section when quadrupole in BC1 is turned on.

Parameter	Value
Average (σ_x, σ_y) in Linac-1	(0.10, 0.10) mm
Average (σ_x, σ_y) in Linac-2	(0.80, 0.05) mm
Average (σ_x, σ_y) in Linac-3	(0.40, 0.02) mm

The average beam sizes through the accelerator are listed in Table III. An effective beam radius $r_b = 2\sqrt{\sigma_x \sigma_y}$ was used in the analytical model.

IV. MULTIPARTICLE SIMULATION WITH COLLECTIVE EFFECTS

The macroparticle simulation in the above benchmark includes only the longitudinal space-charge effect. The effects of transverse space-charge and wakefield and the effects of coherent synchrotron radiation (CSR) in the proposed mitigation scheme were not included. To verify the above scheme, TSC, CSR and the TESLA superconducting cavity transverse structure wakefield effects were added in the following simulations. We simulated an electron beam with an initial 0.1% current modulation at 100 μm wavelength following the initial beam parameters described in Table I. Figures 7 and 8 show the final longitudinal phase space distribution and the projected current profile at the exit of Linac-3 when the quadrupole in BC1 is turned off. Strong energy and current modulations can be seen after two-stage compression due to the microbunching instability.
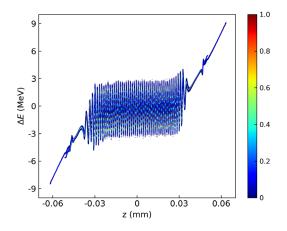

FIG. 7. Final longitudinal phase space with 1st order energy chirp removed when quadrupole in BC1 is turned off.
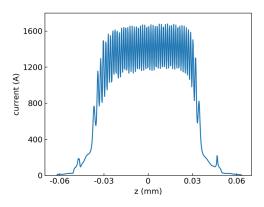

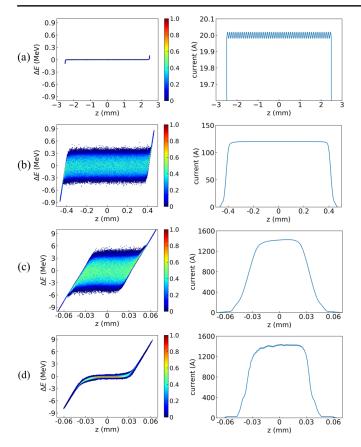FIG. 8. Final current modulation when quadrupole in BC1 is turned off.

FIG. 9. Longitudinal phase space evolution with 1st order energy chirp removed (left) and current profile evolutions (right). (a) at the entrance of BC1, (b), at the exit of BC1, (c), at the entrance of dogleg, (d), at the exit of dogleg.

When the quadrupole in BC1 is turned on, the simulation results of the longitudinal phase space and the current profile at several locations of accelerator beam line are shown in Fig. 9. The initial slice energy spread is assumed to be 2 keV, and is increased to about 160 keV (rms) after the BC1. The induced current modulation is smeared out after the passage through the BC1 as seen in Fig. 9(b). Finally at the exit of dogleg section, inside the core of the electron beam, the induced additional slice energy spread is restored to the nominal one, 144 keV, which is shown in Fig. 9(d) and the right plot of Fig. 10. Due to the additional slice energy spread after the BC1 and the corresponding smearing effects, the current profiles between the BC1 and the dogleg are smooth with little modulation, which shows the suppression of microbunching instability inside the system. A small current modulation is still visible at the exit of dogleg. For a real electron beam, the initial current modulation ($\sim$0.001%) due to electron shot noise can be much smaller than the 0.1% modulation used in the simulation. The current modulation at the exit of the dogleg would be barely noticeable. The final slice emittance is also shown in the left plot of Fig. 10. The normalized slice emittance in the horizontal direction of the beam core section increases by about 6%, while the vertical slice
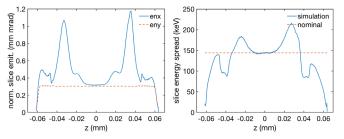

FIG. 10. Final transverse normalized slice emittance (left) and rms slice energy spread (right) when quadrupole in BC1 is turned on.

emittance stays about the same as the initial emittance. Up to 100 million macroparticles with $512 \times 64 \times 512$ grid points were used in the simulation to test the convergence. These results suggest that the effects of transverse space-charge and structure wakefield, and the effects of CSR through the above linear accelerator system could be relatively small. The slice emittance and energy spread outside the electron beam core increase significantly, this is mainly due to the strong space charge effects near the edge of the distribution.

V. CONCLUSIONS

In this paper, we proposed a scheme to mitigate the microbunching instability in a linear accelerator with two bunch compression stages for the x-ray FEL radiation. This scheme has the advantage of suppressing micro-bunching instability but without causing additional final energy spread growth, so-called reversible heater. The horizontal-to-longitudinal coupling due to the insertion of a quadrupole inside the bunch compressor BC1 in this scheme helps smear the initial microbunching and also efficiently suppress the microbunching amplification through the following accelerator sections. Inside the core of electron beam, the final slice energy spread is success-fully restored to the nominal value even when space-charge, CSR and the transverse structure wakefield are taken into account in the simulations. The slice emittance in the core of the beam is also reasonably well preserved at the exit of the dogleg section.

Because of the achromatic lattice design, the current and energy modulations induced before the BC1 cannot be suppressed in this scheme. Considering the short trans-portation distance of Linac-1 section, the contribution to the microbunching instability gain from this section should be relatively small.

One unavoidable effect in this scheme is the beam tilt effect. The transverse-to-longitudinal correlation after the BC1 introduces chromatic effects when transporting par-ticles through accelerator beam line elements such as a quadrupole. Careful lattice design including sextupole mag-nets are needed to correct these nonlinear effects and will be reported in the future study. Furthermore, we would also

like to include the machine imperfections from realistic optics in the future study.

ACKNOWLEDGMENTS

[1] M. Borland *et al.*, Start-to-end simulation of self-amplified spontaneous emission free electron lasers from the gun through the undulator, Nucl. Instrum. Methods Phys. Res., Sect. A **483**, 268 (2002).

[2] S. Heifets, G. Stupakov, and S. Krinsky, Coherent synchrotron radiation instability in a bunch compressor, Phys. Rev. Accel. Beams **5**, 064401 (2002).

[3] Z. Huang and K.-J. Kim, Formulas for coherent synchrotron radiation microbunching in a bunch compressor chicane, Phys. Rev. Accel. Beams **5**, 074401 (2002).

[4] E. L. Saldin, E. A. Schneidmiller, and M. V. Yurkov, Longitudinal space charge-driven microbunching instability in the TESLA Test Facility linac, Nucl. Instrum. Methods Phys. Res., Sect. A **528**, 355 (2004).

[5] Z. Huang, M. Borland, P. Emma, J. Wu, C. Limborg, G. Stupakov, and J. Welch, Suppression of microbunching instability in the linac coherent light source, Phys. Rev. Accel. Beams **7**, 074401 (2004).

[6] M. Venturini, Microbunching instability in single-pass systems using a direct two-dimensional Vlasov solver, Phys. Rev. Accel. Beams **10**, 104401 (2007).

[7] R. A. Bosch, K. J. Kleman, and J. Wu, Modeling two-stage bunch compression with wakefields: Macroscopic properties and microbunching instability, Phys. Rev. Accel. Beams **11**, 090702 (2008).

[8] J. Qiang, R. D. Ryne, M. Venturini, A. A. Zholents, and I. V. Pogorelov, High resolution simulation of beam dynamics in electron linacs for x-ray free electron lasers, Phys. Rev. Accel. Beams **12**, 100702 (2009).

[9] S. Di Mitri, M. Cornacchia, S. Spampinati, and S. Milton, Suppression of microbunching instability with magnetic bunch length compression in a linac-based free electron laser, Phys. Rev. Accel. Beams **13**, 010702 (2010).

[10] S. Seletskiy, B. Podobedov, Y. Shen, and X. Yang, Seeding, Controlling, and Benefiting from the Microbunching Instability, Phys. Rev. Lett. **111**, 034803 (2013).

[11] S. Di Mitri and S. Spampinati, Microbunching Instability Suppression via Electron-Magnetic-Phase Mixing, Phys. Rev. Lett. **112**, 134802 (2014).

[12] D. Ratner, C. Behrens, Y. Ding, Z. Huang, A. Marinelli, T. Maxwell, and F. Zhou, Time-resolved imaging of the microbunching instability and energy spread at the Linac Coherent Light Source, Phys. Rev. Accel. Beams **18**, 030704 (2015).

[13] C.-Y. Tsai, D. Douglas, R. Li, and C. Tennant, Linear microbunching analysis for recirculation machines, Phys. Rev. Accel. Beams **19**, 114401 (2016).

[14] J. Qiang, Y. Ding, P. Emma, Z. Huang, D. Ratner, T. O. Raubenheimer, M. Venturini, and F. Zhou, Start-to-end simulation of the shot-noise driven microbunching instability experiment at the Linac Coherent Light Source, Phys. Rev. Accel. Beams **20**, 054402 (2017).

[15] Z. Huang, A. Brachmann, F.-J. Decker, Y. Ding, D. Dowell, P. Emma, J. Frisch, S. Gilevich, G. Hays, and P. h. Hering, Measurements of the linac coherent light source laser heater and its impact on the x-ray free-electron laser performance, Phys. Rev. Accel. Beams **13**, 020703 (2010).

[16] L. H. Yu, Generation of intense uv radiation by subharmonically seeded single-pass free-electron lasers, Phys. Rev. A **44**, 5178 (1991).

[17] J. Qiang, C. E. Mitchell, and M. Venturini, Suppression of Microbunching Instability Using Bending Magnets in Free-Electron-Laser Linacs, Phys. Rev. Lett. **111**, 054801 (2013).

[18] C. Behrens, Z. Huang, and D. Xiang, Reversible electron beam heating for suppression of microbunching instabilities at free-electron lasers, Phys. Rev. Accel. Beams **15**, 022802 (2012).

[19] C. Feng, D. Huang, H. Deng, Q. Gu, and Z. Zhao, New J. Phys. **17**, 073028 (2015).

[20] D. Huang, C. Feng, H. Deng, Q. Gu, and Z. Zhao, Transverse to longitudinal phase space coupling in an electron beam for suppression of microbunching instability, Phys. Rev. Accel. Beams **19**, 100701 (2016).

[21] T. Liu, W. Qin, D. Wang, and Z. Huang, Reversible beam heater for suppression of microbunching instability by transverse gradient undulators, Phys. Rev. Accel. Beams **20**, 082801 (2017).

[22] Z. Huang and G. Stupakov, Control and application of beam microbunching in high brightness linac-driven free electron lasers, Nucl. Instrum. Methods Phys. Res., Sect. A **907**, 182 (2018).

[23] P. Emma *et al.*, Experimental Demonstration of Energy-Chirp Control in Relativistic Electron Bunches Using a Corrugated Pipe, Phys. Rev. Lett. **112**, 034801 (2014).

[24] H. X. Deng *et al.*, Experimental Demonstration of Longitudinal Beam Phase-Space Linearizer in a Free-Electron Laser Facility by Corrugated Structures, Phys. Rev. Lett. **113**, 254802 (2014).

[25] G. Stupakov and P. Emma, *Proceedings of FEL 2015, Daejon, Korea*, 2015, http://accelconf.web.cern.ch/AccelConf/FEL2015/papers/mop056.pdf.

[26] M. Borland, Elegant: A flexible sdds-compliant code for accelerator simulation, Argonne National Lab. Report No. LS-287, 2000.

[27] J. Qiang, R. D. Ryne, S. Habib, and V. Decyk, An object-oriented parallel particle-in-cell code for beam dynamics simulation in linear accelerators, J. Comput. Phys. **163**, 434 (2000).

[28] J. Qiang, S. Lidia, R. D. Ryne, and C. Limborg, Three-dimensional quasistatic model for high brightness beam dynamics simulation, Phys. Rev. Accel. Beams **9**, 044204 (2006).

[29] M. Borland, Modeling of the microbunching instability, Phys. Rev. Accel. Beams **11**, 030701 (2008).